Atomic scale determination of cation inversion in spinel-based oxide nanoparticles.

Pau Torruella[1,2,*], Alicia Ruiz-Caridad[1,2,3], Michael Walls[3], Alejandro G. Roca[4], Alberto López-Ortega[5], Javier Blanco-Portals[1,2], Lluís López-Conesa[1,2,6], Josep Nogués[4,7], Francesca Peiró[1,2], Sònia Estradé[1,2].

[1] LENS-MIND, Departament d'Enginyeria Electrònica i Biomèdica, Universitat de Barcelona, E-08028 Barcelona, Spain.

[2] Institute of Nanoscience and Nanotechnology (IN2UB), Universitat de Barcelona, E-08028 Barcelona, Spain.

[3] Laboratoire de Physique des Solides, Paris-Sud University, France

[4] Catalan Institute of Nanoscience and Nanotechnology (ICN2), CSIC and BIST, Campus UAB, Bellaterra, E-08193 Barcelona, Spain

[5] CIC nanoGUNE, Tolosa Hiribidea, 76, E-20018 Donostia-San Sebastián, Gipuzkoa, Spain

[6]TEM-MAT,CCiT, Universitat de Barcelona, E-08028 Barcelona, Spain.

[7] ICREA, Pg. Lluís Companys 23, E-08010 Barcelona, Spain.

* Corresponding autor: P. Torruella, e-mail: ptorruella@el.ub.edu

Abstract

The atomic structure of nanoparticles can be easily determined by transmission electron microscopy. However, obtaining atomic resolution chemical information about the individual atomic columns is a rather challenging endeavor. Here, crystalline monodispersed spinel Fe_3O_4/Mn_3O_4 core/shell nanoparticles have been thoroughly characterized in a high-resolution scanning transmission electron microscope (STEM). Electron Energy-Loss Spectroscopy (EELS) measurements performed with atomic resolution allow direct mapping of the Mn^{2+}/Mn^{3+} ions in the shell and the Fe^{2+}/Fe^{3+} in the core structure. This enables a precise understanding of the core/shell interface and of the cation distribution in the crystalline lattice of the nanoparticles. Considering how the different oxidation states of transition metals are reflected in EELS, two methods to perform a local evaluation of the cation inversion in spinel lattices are introduced. Both methods allow determining the inversion parameter in the iron oxide core and manganese oxide shell, as well as detecting spatial variations in this parameter, with atomic

resolution. X-ray absorption measurements on the whole sample confirm the presence of cation inversion. These results present a significant advance towards a better correlation of the structural and functional properties of nanostructured spinel oxides.

Keywords: Magnetic Nanoparticles, EELS, Core-Shell, Spinel, Cation Inversion.

Introduction

Nanoparticles are gaining increased interest owing to their numerous applications in widespread fields[1–4]. Spinel oxides have been frequently used in nanoparticle synthesis due to the appealing fundamental properties linked to their unique structure, with uses ranging from everyday materials, like ceramics, to advanced applications in biotechnology[5–9]. In fact, given the structural similarities, spinel materials are particularly suited to grow core/shell structures with enhanced multifunctional properties[10–17].

Spinel materials are characterized by an AB_2Z_4 structure, where A and B are divalent and trivalent cations, respectively, and Z is a divalent anion, typically oxygen. The A cations occupy the tetrahedral positions (T_h) in the structure, whereas the B cations occupy the octahedral (O_h) ones. However, depending on the nature of the A and B cations (e.g., ionic radius) and the external conditions (e.g., temperature or pressure) the distribution of the cations in the structure can be altered. This distribution is characterized by the degree of inversion, *x*, where the structure is represented as $(A_{1-x}B_x)[A_xB_{2-x}]Z_4$, where "( )" denote T_h positions in the structure and "[ ]" O_h positions, respectively. Thus, normal spinels, $(A)[B_2]Z_4$, have $x = 0$, a material with a completely inverted structure, i.e., $(B)[AB]_2Z_4$, would have $x = 1$ and is called an inverse spinel, while x is equal to $^2/_3$ for a completely random cation distribution[18]. Although, the different spinel materials are normally classified in specific spinel categories (e.g., $FeAl_2O_4$ is a normal spinel), depending on different factors such as the synthesis approach (e.g., thermal decomposition, sol-gel), processing methods (e.g., quenching, ball-milling), morphology (e.g., thin films, nanoparticles) or size, a cation inversion different from the nominal one can take place, leading to a change in the inversion parameter with respect to bulk materials. Interestingly, the degree of inversion has been shown to play an important role in the functional properties (e.g., electronic, transport, optical, magnetic, mechanical or structural) of spinel materials[19–27]. However, despite its relevance, the inversion parameter is seldom studied in detail, particularly in nanostructured materials. Several techniques exist that can assess the coordination of chemical species in a crystal, such as x-ray and neutron diffraction refinement, Mössbauer spectroscopy, x-ray absorption or nuclear magnetic resonance[28–31]. In general, these techniques yield averaged information, typically from rather

large volumes. Nonetheless, when dealing with complex systems such as core/shell nanoparticles, a few unit cells can determine the resulting overall properties of the system, often making classical bulk approaches unsuitable. In fact, the atomic scale determination of the inversion parameter has never been reported. Therefore, it is clear that novel approaches are required to selectively characterize the different ions in nanoparticles with high spatial resolution.

In this framework, aberration-corrected transmission electron microscopy (TEM) is an extremely useful technique to probe materials at the atomic scale. Moreover, when coupled to electron energy-loss spectroscopy (EELS), the oxidation state of chemical species[23–27] and their distribution in a crystalline lattice can be mapped[32,33].

Here we report on the atomic resolution study of the oxidation state and the cation inversion parameter in Fe_3O_4/Mn_3O_4 core/shell nanoparticles. State of the art statistical methods are used in order to determine the oxidation state of individual atomic columns. Interestingly, coordination inversion is determined in each individual atomic column. These measurements, unprecedented in such small nanosystems, can be crucial in the understanding of the functional properties of nanoparticles.

Methods

Synthesis

The Fe_3O_4/Mn_3O_4 core/shell nanoparticles were synthesized using a seed-growth approach. Fe_3O_4 nanoparticles were previously synthesized and used as seeds for the subsequent growth of the Mn_3O_4 shells[11,32].

The Fe_3O_4 seeds were synthesized by thermal decomposition of iron(III) oleate in 1-octadecene in the presence of oleic acid. 1.82 g (2mmol) iron(III) oleate and 0.1 g (0.4 mmol) oleic acid were dissolved in 20 mL of 1-octadecene. The reaction mixture was heated up to 320 ºC with a heating rate of 3 ºC/min under argon flow and kept at this temperature for 30 min. The reaction mixture was then cooled down to room temperature. The purification process subsequently involves several centrifugation cycles with a mixture of hexane and ethanol. Finally, the particles were dispersed in hexane. The subsequent growth of a Mn_3O_4 layer onto the Fe_3O_4 seeds was performed by dispersing 200 mg of Fe_3O_4 nanoparticles and 0.1 g (0.4 mmol) of oleic acid in 40 mL of dibenzyl ether, degassed under several cycles of vacuum/argon to remove any hexane traces. Then, the suspension was heated up to 220 ºC under an argon flow. At this moment, a solution of 0.2 g (0.6 mmol) of manganese(II) acetylacetonate, 0.2 g (2 mmol) of 1,2-hexadecanediol and 0.8 g (3 mmol) of oleylamine, previously heated up to 100 ºC, was injected at fast rate. The reaction mixture was kept at 220 ºC for 60 min and then cooled down to room temperature. The core/shell nanoparticles were purified several times by magnetic separation after mixing with hexane and acetone.

TEM characterization

For the TEM observation the samples were dispersed in hexane and, after 30 min sonication, were deposited on a holey-carbon coated copper grid.

Scanning TEM high angle annular dark field images (STEM-HAADF) and EELS spectrum images were acquired in an aberration-corrected Nion UltraSTEM200 TEM equipped with a cold field emission gun and a Gatan Enfina high-resolution EELS spectrometer. The experiments were performed at 100kV. The convergence and collection angles for spectroscopy were 35 and 80 mrad respectively. The beam current was between 40-60 pA for all spectrum images.

EELS analysis was performed in python using the open-source EELS analysis suite *Hyperspy*[34,35] and the Gatan Digital Micrograph software.

X-ray Absorption Spectroscopy

The room temperature x-ray absorption spectra at the Fe and Mn $L_{2,3}$-edges were acquired in total electron yield mode at the BM-26 beamline (BOREAS) of the ALBA-CELLS synchrotron. The spectra were fitted using the CTM4XAS program[36].

Results

STEM-HAADF images (Figure 1A-B) show rounded monodisperse particles exhibiting a 14.7 nm average size and a standard deviation of 1.2 nm (Figure 1C). EEL-Spectrum Imaging at high resolution for the region in figure 1D reveals the core/shell nature of the nanoparticles. Oxygen, iron and manganese quantification maps (Figures 1E-G), demonstrate that the nanoparticles are composed of iron oxide cores surrounded by irregular manganese oxide shells with a 1-2 nm thickness (Figure 1H). From measurements in the elemental quantification maps of several nanoparticles, the core/shell interface was found to extend 0.31 ± 0.05 nm (Figure S1), which can be considered as atomically sharp. The observed oxygen relative composition[37] is around 58% (Figure S2), which is only compatible with a magnetite (Fe_3O_4) core. In concordance with these measurements, hausmannite (Mn_3O_4) is the most likely phase of the manganese oxide shell. This was further studied by analyzing the fine structure of the Mn $L_{2,3}$-edge. An EELS spectrum acquired over several nanoparticles was analyzed using our open source code OxideWizard and also compared to reference data,[38,39] demonstrating that the shell is indeed hausmannite (Figure S3-4).

The detailed structural analysis from atomic resolution STEM-HAADF images shows that the manganese oxide shell is a tetragonal spinel phase[40] while the iron oxide core is a cubic spinel phase[41] (Figure S5). From these $[100]Mn_3O_4//[110]Fe_3O_4$ zone axis views, the planes of the interface between the core and the shell are $(001)Fe_3O_4//(001)Mn_3O_4$ and in the perpendicular direction $[1\text{-}10]Fe_3O_4$ is parallel to $[010]Mn_3O_4$, resulting in the $(001)[1\text{-}10]Fe_3O_4//(001)[010]Mn_3O_4$ epitaxial relationship between the core and the shell (see details in in the Supplementary Information, SI; Figures S5-7), in agreement with other Fe_3O_4/Mn_3O_4 growth studies[42]. This crystallographic adaptation of the crystals has an associated mismatch of 3.3% (see SI), which probably leads to some of the planar crystal defects observed in Figure S8.

EELS $L_{2,3}$-edge intensity maps (Figure 2) of the nanoparticle oriented along a high symmetry zone axis (survey image at low magnification in figure S9) further confirm the spinel structure of both the magnetite core and the hausmannite shell. Figure 2A corresponds to the HAADF image of the nanoparticle in [100]Mn_3O_4/[110]Fe_3O_4 zone axis orientation and Figures 2B-D present the EELS elemental maps at atomic resolution in the shell (Figure 2C) and the core (Figure 2D), respectively. From these images it was possible to understand the core/shell interface at the atomic level, schematically shown in Figures 2E,F. However, to gain further insight into the intimate configuration of these nanoparticles, the location of 2+ and 3+ species of each element in the different oxygen coordination sites must be unveiled.

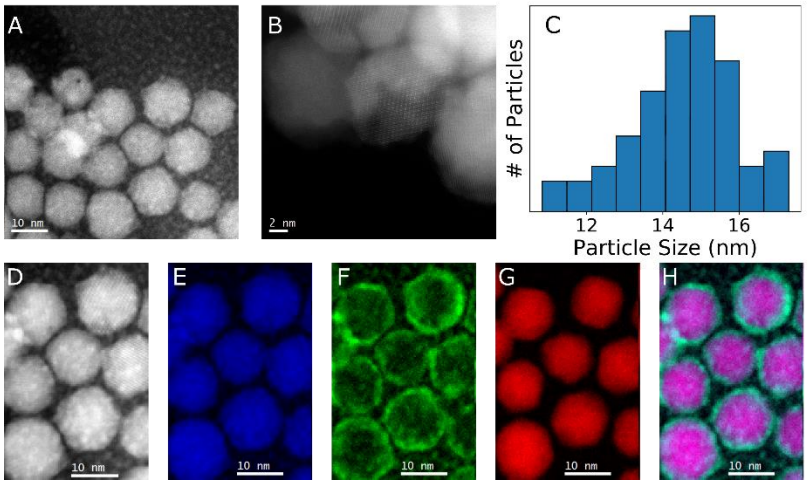

Figure 1. STEM-HAADF and EELS characterization of the nanoparticles A) at medium resolution and B) at higher resolution. C) Size distribution of the nanoparticles, obtained from STEM-HAADF images. D) STEM-HAADF image from the region where EELS spectrum imaging was performed to map the E) oxygen signal, F) manganese signal and G) iron signal. H) Color mix of panels E-G.

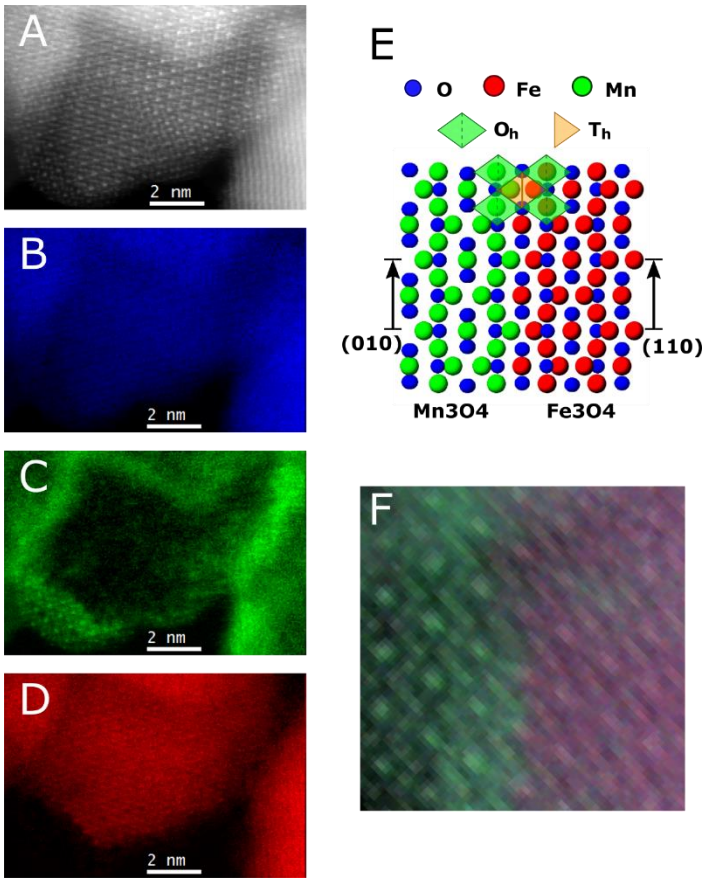

Figure 2. EELS spectrum imaging of the nanoparticles at atomic resolution. A) HAADF survey image. Integrated EELS signal from the B) O K-edge, C) $FeL_{2,3}$-edge and D) Mn $L_{2,3}$-edge. E) Atomistic model of the core/shell interface. F) Superposition of the O, Fe, Mn and HAADF signals at the interface.

One possible way to obtain an oxidation state mapping is through the analysis of the energy-loss near edge structures (ELNES) related to a given element[39,43–45]. Potentially, these ELNES features allow the determination of divalent/trivalent cation lattice distribution from spectrum images acquired at sufficient energy and spatial resolution. In many transition metals the ELNES display two sharp peaks (L_3 and L_2), often referred to as white lines, where the associated ELNES parameters are the onset of the peaks, their relative position or their relative intensity. In the particular case of manganese, the determination of the oxidation state is carried out by using the Mn L_3/Mn L_2 intensity ratio and the onset of the Mn L_3 peak[38,44,46]. On the other hand, for iron, the onset of the Fe L_3-edge has been reported to shift to higher energies as its oxidation state increases from Fe^{2+} to Fe^{3+} [45,47–49].

Interestingly, these ELNES features allow the calculation of the cation inversion, provided that spectra from individual atomic columns can be obtained. In particular, the following expression, valid for most transition metal spinel oxides, can be used to calculate the cation inversion parameter:

$$x = \frac{2}{3}\left(1 - C\frac{S}{S_{ref}}\right) \quad (1)$$

where S is the measured L_3 shift between two atomic columns and S_{ref} and C are parameters related to the particular element that is being considered and the zone axis in which the crystal lattice is measured (the details of the derivation are provided in the Supplementary Information).

This approach was pursued with the spectrum image shown in Figure 3. Figure 3A shows an atomic resolution STEM-HAADF image. The particle is oriented along a low symmetry zone axis: [541] (the plane indexation of the image can be found in Figure S10). An atomic resolution EELS spectrum image was acquired from the highlighted region of panel A, which shows the expected (111) planes in this zone axis (Figure 3B). Notably, the (111) planes of magnetite (labeled with numbers in the image) contain iron atoms only in octahedral coordination (12 per unit cell). On the other hand, between these planes, in the regions with darker contrast in Figure 3B, iron atoms are distributed in both octahedral and tetrahedral coordination (8 T_h and 4 O_h positions per unit cell; Figure 3C). The bright planes have been labeled with a number (*i*), in figure 3B-C while the darker planes will be referred as *i'*.

A spectrum image was acquired from the region displayed in figure 3B. To improve the signal to noise ratio, and given the symmetry in the image, spectra were added along the vertical direction to obtain a spectrum line (displayed in figure 3D), where the horizonal axis is the same as in figure 3B and the vertical one corresponds to the energy loss. As an example, the spectra corresponding to positions 5(5´) (highlighted in blue(orange) in Figure 3D) are plotted in Figure 3E. The onset of the Fe L3 edge was calculated as the energy at which half the intensity of the peak was attained. The variation of the Fe L3 onset along the direction [111] is plotted in Figure 3F (blue line). A shift is observed between adjacent *i-i'* of planes, as can be observed in the example of Figure 3E, which demonstrates an uneven distribution of iron ions with different oxidation states. This Fe L_3 shift between the two types of planes was calculated to be of 0.3 eV on average (see S11).

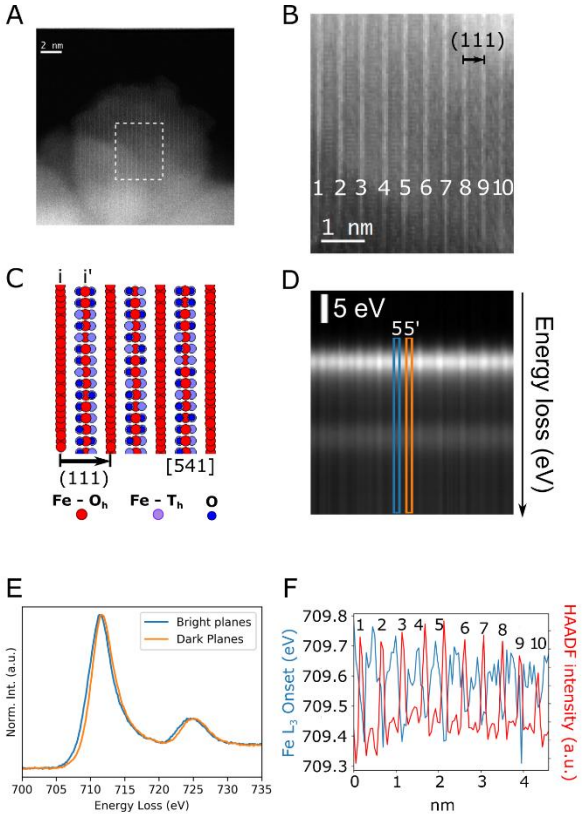

Figure 3. Fe_3O_4 core ELNES mapping. A) STEM-HAADF image. B) STEM-HAADF signal co-acquired with an EELS spectrum image from the highlighted region in panel A. C) corresponding atomistic model of magnetite along the observed zone axis. D) Plot of the spectrum line obtained by vertical addition of the spectra. E) EELS spectra extracted from the positions 5 and 5'. A shift of L3 is observed. F) Profiles of the iron L_3 onset along the direction [111] and the the corresponding HAADF signal from.

From this measurement, expression (1) can be applied to calculate the cation inversion parameter of the magnetite core in the nanoparticle. After taking S_{ref} = 1.7 eV from [47] and C = -3/2 from the analyzed planes, the inversion parameter of the iron oxide core was found to be x = 0.84 ± 0.02, where the error was estimated from the standard deviation of the Fe L_3 shifts.

A similar approach was used to calculate the inversion parameter of the hausmannite shell. Figure 4A shows an enlarged view of the Mn_3O_4 shell of the same nanoparticle as in Figure 2. The comparison with the atomistic model (Figure 4B) demonstrates that, in this orientation, the observed atomic columns contain exclusively either ions in tetrahedral coordination (orange) or in octahedral coordination (green). The Mn L_3 onset was mapped, as shown in Figure 5A, where regions with low Mn signal (the Fe_3O_4 core and vacuum) have been masked. A histogram of the Mn L_3 energy onset in pixels corresponding to columns of tetrahedral and octahedral coordination is shown in Figure 5B. The tetrahedral/octahedral column positions where manually chosen from the correlated HAADF image.

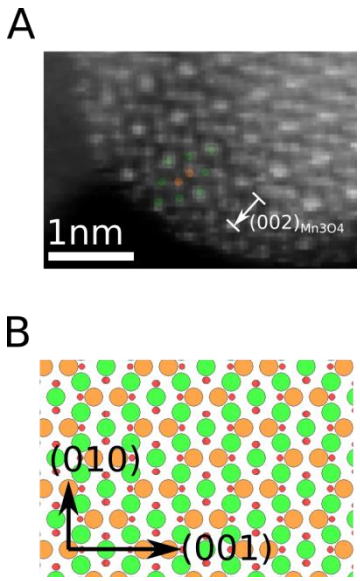

Figure 4. Mn_3O_4 shell lattice. A) Close up of Figure 2A on the manganese oxide shell, where the atomic columns containing Mn atoms in exclusively tetrahedral or exclusively octahedral coordination are marked in orange and green, respectively. The direction and extent of the (002)Mn_3O_4 planes have been highlighted. B) Model of the hausmannite crystal lattice seen in the [100]Mn_3O_4 zone axis. Mn ions in tetrahedral coordination are shown in orange and those in octahedral coordination in green.

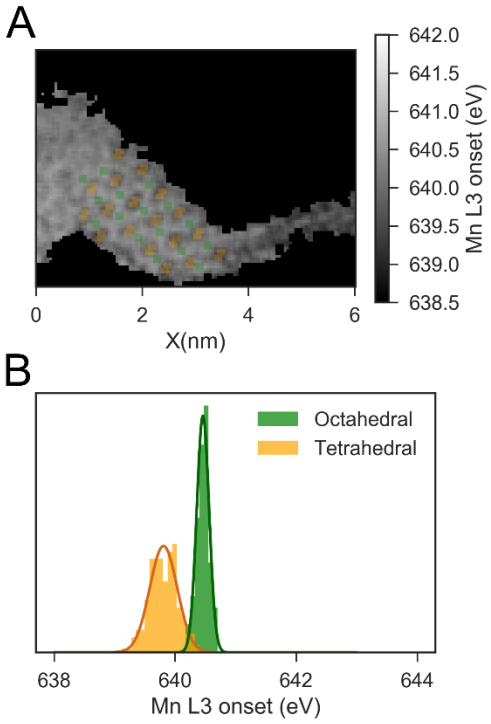

Figure 5. Mn L_3 onset distribution. A) Mn L_3 energy onset. Note that in A), regions of low Mn signal have been masked. Overlaid in green and orange, are the pixel selections for cation atomic columns with either tetrahedral or octahedral oxygen coordination. B) Histogram of the Mn L_3 energy onset for the selected pixels in panel A.

The centers of the distribution of the Mn L_3 energy onsets are shifted 0.65 eV between octahedral and tetrahedral Mn coordination. From this measurement, the cation inversion parameter was calculated to be x = 0.39 ± 0.10, using C = 1 for the treated zone axis and atomic columns and S_{ref} = 1.6.[46] The cation inversion uncertainty has been estimated from the width of the EELS energy onsets distributions of Figure 5B. It should be noted that the uncertainty in this measurement is much larger than for the one corresponding to magnetite.

An alternative way to unravel the contribution of the different cations in each crystallographic site can be considered. Multivariate analysis (MVA) and spectral decomposition techniques have been used in the past to obtain maps related to the density of a specific ion[34,50,51]. If such maps are obtained at atomic resolution, for a spinel crystal the cation inversion can be estimated simply as the fraction of signal from the 3+ ion at the tetrahedral coordination positions:

$$x = \left(\frac{I_{3+}}{I_{3+} + I_{2+}}\right)_{T_h} \quad (2)$$

Principal component analysis (PCA) was applied to the spectrum image shown in Figure 2 for the energy range corresponding to the Mn $L_{3,2}$-edge. The results revealed that 3 components were enough to describe the whole dataset (Figure S12). Then, a 3-component spectral decomposition was performed through Non-negative Matrix Factorization (NMF)[52], yielding the components depicted in Figure 6A. The component C0 has no relevant spectral features, and is considered a background, basically related to the thickness at each point of the image. On the other hand components C1 and C2 show Mn L-edges with very distinct features. In particular, the L_3/L_2 intensity ratio is much higher for C1 than for C2 and the L_3 peak is at lower energies for C1 than for C2. By further comparison with reference spectra[44,46,49] it is possible to assign C1 to be proportional to the Mn^{2+} ion density and C2 to the Mn^{3+} ion density. The score maps for the three individual components are shown in Figure S13. In Figure 6B, the score maps of C1 (orange color scale) and C2 (green color scale) are combined, highlighting the Mn^{2+} and Mn^{3+} sublattices. The maps have an excellent correspondence with the different oxygen coordination sites, similarly to previously atomic resolution EELS maps obtained through multilinear least square fitting in hausmanite[33], with the map of C1 and C2 having higher intensity in the T_h and the O_h sites, respectively (Figure 6B).

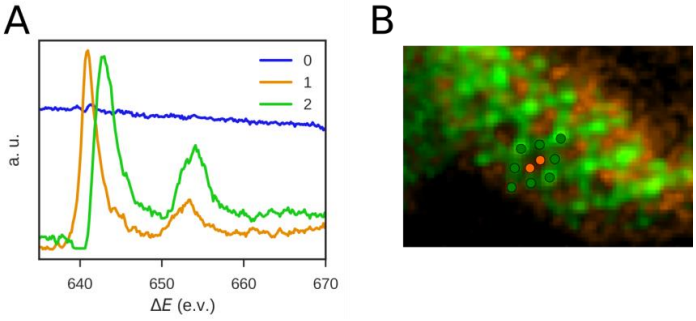

Figure 6. Mn L-edge spectral decomposition. A) Non-negative Matrix Factorization components of the Mn L-edge in the Figure 4 spectrum image. B) Color composition of component 1 (orange) and component 2 (green) score maps.

Once the maps proportional to the Mn^{2+} (C1) and Mn^{3+} (C2) are obtained, they must be normalized so that Equation 2 can be reliably used. In this case, each map was divided by the integrated signal of their corresponding spectrum. The resulting information is plotted in Figure 7. Figure 7A shows an image of the manganese oxidation state, calculated by the weighted average of 2+ and 3+ ions $\frac{2I_{Mn_{2+}}+3I_{Mn_{3+}}}{I_{Mn_{2+}}+I_{Mn_{3+}}}$. The inversion parameter is displayed as a color-coded spot over each atomic column of tetrahedral coordination. The x values range between 0.2 and 0.45, with an atomic column frequency distribution (Figure 7B) centered at about x = 0.35, in quite good agreement with the results obtained from the previous approach.

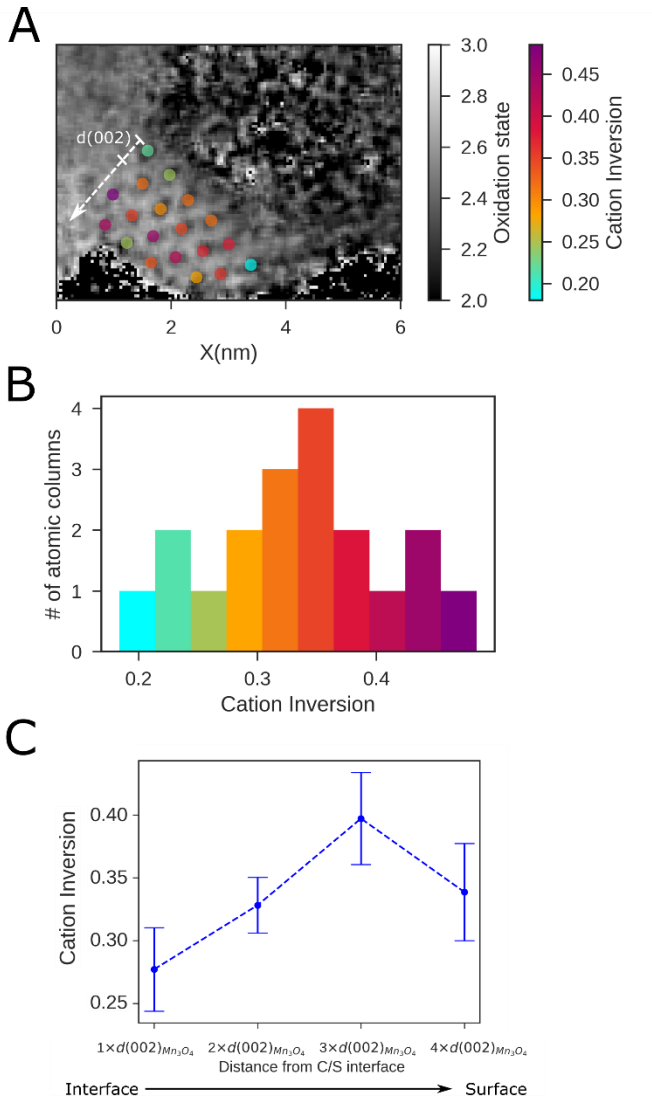

Figure 7. Cation inversion for tetrahedral atomic columns. A) Mn oxidation state map in grayscale. The calculated inversion parameters are displayed, color coded, over their corresponding atomic column. B) Frequency histogram of the calculated inversion parameters

from panel A. C) Inversion parameter of hausmannite vs. distance from the core/shell (C/S) interface measured in number of (002) planes [d(002)=4.7Å]. The error bars were determined as the standard deviation of the values for each plane.

Interestingly, the measurements shown in Figure 7 allow the observation of an "inversion gradient" from the core/shell interface to the surface of the particle. The spatial variation can be better observed if the inversion parameter for the tetrahedral atomic columns is averaged for each (002)Mn_3O_4 plane (Figure 7C). It can be clearly observed that x is smaller closer to the interface than at the surface of the nanoparticle.

Remarkably, x-ray absorption experiments (a well-stablished method to asses cation coordination inversion[53–55]) on the nanoparticle powder samples confirm the presence of cation inversion in Mn_3O_4, with a stoichiometry of about $(Mn^{2+}_{0.56}\ Mn^{3+}_{0.44})_{Td}\ [Mn^{2+}_{0.44}\ Mn^{3+}_{1.56}]_{Oh}O_4$, i.e., $x \sim 0.44$ (see Figure S14a and Table S1), in reasonable agreement with the atomic scale cation inversion. Similarly, for Fe_3O_4, some degree of cation inversion is also observed, with $(Fe^{2+}_{0.14}\ Fe^{3+}_{0.86})_{Td}\ [Fe^{2+}_{0.86}\ Fe^{3+}_{1.14}]_{Oh}O_4$, i.e., $x \sim 0.86$ (see Figure S14b and Table S2). The small differences in cation inversion between the two techniques probably stem from the statistical average character of the x-ray absorption and to a certain extent from the somewhat non-univocal nature of the x-ray absorption fits.

Discussion

In this work two main objectives have been pursued: (i) the thorough characterization of Fe_3O_4/Mn_3O_4 core/shell nanoparticles at the atomic scale has been achieved, and (ii) two different methods to calculate the cation inversion parameter of spinel crystals with unprecedented spatial resolution have been demonstrated. These methods will be referred to as the "ELNES" approach, associated with Equation (1) and demonstrated in Figures 3 and 5, and the "MVA" approach, associated with Equation (2) with the corresponding results shown in Figures 6-7.

The iron oxide cores have been found to be Fe_3O_4, i.e., nominally, an inverse spinel with $x = 1$. However, the cation inversion parameter of the iron oxide core was found to be $x = 0.84 \pm 0.02$ through the ELNES analysis approach. Although this value is smaller than that expected for Fe_3O_4, this is not overly surprising, since magnetite nanoparticles, prepared by different methods, with inversion parameters lower than 1 have already been reported[56,57]. This cation inversion can stem from different factors such as structural defects, surface effects or iron vacancies in the lattice.

The cation inversion for the hausmannite shell has been evaluated to be $x = 0.39 \pm 0.10$ following the ELNES analysis approach. However, the rather broad distribution of the Mn L_3 energy onset leads to a high uncertainty in the value of the cation inversion parameter ($\Delta x = 0.10$). Actually, the MVA approach, depicted in Figures 7, evidenced that this uncertainty is related to a spatial variation of the cation inversion rather than an intrinsic lack of precision of the method. This illustrates a possible drawback of the ELNES approach. Namely, the inversion is measured relative to, at least, two different atomic columns and, therefore, it is not possible to determine the x values with a higher resolution than the distance between the two

columns. Moreover, the two different atomic columns used to calculate S are unavoidably chosen arbitrarily in this approach. Additionally, the evaluation of the inversion through Equation (1) requires a reference value (S_{ref}) for the energy shift of an edge related to the oxidation state of a given element. Nonetheless, reference spectra are available for most elements that can be found in a spinel lattice. Finally, the assumption of a linear dependence between onset shift and oxidation state may not always hold, although Equation (1) may be adapted to higher order dependences.

Remarkably, all of these issues are avoided with the spectral decomposition ("MVA") approach. As shown in figures 7, cation inversion measurements with true atomic resolution can be achieved through Equation (2) with the only limitation being the ability to obtain a sufficiently good spectral decomposition. The average x value obtained by this approach is consistent with the one from the ELNES approach. However, it is worth emphasizing that the MVA approach has allowed the unprecedented observation of an atomic resolution spatial variation in the cation inversion in the hausmannite shell (Figure 7C).

Although the origin of this spatial variation is not clear at present, it may lie in the fact that the hausmannite is actually stressed, as it grows epitaxially onto the magnetite as shown in Figures S5-7. In fact, cation inversion can act as an accommodation mechanism. As for the inversion drop at the surface of the nanoparticle, surface reordering of the free bonds does surely affect the electronic environment of the lattice and may also play a role in how the Mn^{2+}/Mn^{3+} populations are distributed. Similarly, the vacancy distribution (which could affect x) in the Mn_3O_4 may be different at the interface than at the surface.

Conclusions

Precise determination of the oxidation state of iron and manganese in an Fe_3O_4/Mn_3O_4 core/shell nanoparticle has been performed. The analysis of the oxidation states, using either by ELNES or MVA approaches, has enabled the first determination of the cation inversion at atomic column resolution from a spinel oxide. The obtained mean cation inversion value for the magnetite core is x = 0.84, whilst for hausmannite it is x = 0.39 (confirmed by x-ray absorption measurements in the whole sample). The analysis also reveals that while the cation inversion in the Fe_3O_4 core is spatially uniform, in the Mn_3O_4 shell it exhibits a decrease in inversion close to the core/shell interface. These novel approaches set the stage for further exploration of oxide nanosystems through EELS at a very high resolution, which should lead to an improved control of the physiochemical properties of these materials.

Acknowledgments

The authors acknowledge funding from the Spanish Ministerio de Economía y Competitividad (MINECO) through the projects MAT2016-77391-R and MAT2016-79455-P / FEDER (UE). This work has also been carried out in the framework of the projects 2017-SGR-292 and 2017-SGR-776 from the Generalitat de Catalunya. ALO acknowledges the MINECO through the Juan de la Cierva Program (IJCI-2014-21530). MW acknowledges the European Union Seventh Framework Programme under Grant Agreement No.312483-ESTEEM2. ICN2 is funded by the CERCA

Programme/Generalitat de Catalunya. ICN2 also acknowledges support from the Severo Ochoa Program (MINECO, grant SEV-2013-0295). We also acknowledge the ALBA Synchrotron Light Facility for the provision of synchrotron beamtime and Dr. J. Herrero (ALBA) for useful discussions.

Supporting Information Available: Derivation of equation (1), Crystalline analysis and spectral analysis details.

References

(1) Zhang, C.; Ni, D.; Liu, Y.; Yao, H.; Bu, W.; Shi, J. *Nat. Nanotechnol.* **2017**, *12*, 378–386.

(2) Zhao, W.; Liu, Z.; Sun, Z.; Zhang, Q.; Wei, P.; Mu, X.; Zhou, H.; Li, C.; Ma, S.; He, D.; Ji, P.; Zhu, W.; Nie, X.; Su, X.; Tang, X.; Shen, B.; Dong, X.; Yang, J.; Liu, Y.; Shi, J. *Nature* **2017**, *549*, 247–251.

(3) Lim, J.; Park, Y.-S.; Klimov, V. I. *Nat. Mater.* **2018**, *17*, 42–49.

(4) Zalineeva, A.; Baranton, S.; Coutanceau, C.; Jerkiewicz, G. *Sci. Adv.* **2017**, *3*, e1600542.

(5) Zhang, K.; Han, X.; Hu, Z.; Zhang, X.; Tao, Z.; Chen, J. *Chem. Soc. Rev.* **2015**, *44*, 699–728.

(6) Gawande, M. B.; Goswami, A.; Felpin, F. X.; Asefa, T.; Huang, X.; Silva, R.; Zou, X.; Zboril, R.; Varma, R. S. *Chem. Rev.* **2016**, *116*, 3722–3811.

(7) Reddy, D. H. K.; Yun, Y. S. *Coord. Chem. Rev.* **2016**, *315*, 90–111.

(8) Lima-Tenório, M. K.; Tenório-Neto, E. T.; Hechenleitner, A. A. W.; Fessi, H.; Pineda, E. A. G. *J. Colloid Sci. Biotechnol.* **2016**, *5*, 45–54.

(9) Naoi, K.; Naoi, W.; Aoyagi, S.; Miyamoto, J. I.; Kamino, T. *Acc. Chem. Res.* **2013**, *46*, 1075–1083.

(10) Sanna Angotzi, M.; Musinu, A.; Mameli, V.; Ardu, A.; Cara, C.; Niznansky, D.; Xin, H. L.; Cannas, C. *ACS Nano* **2017**, *11*, 7889–7900.

(11) Estrader, M.; López-Ortega, A.; Estradé, S.; Golosovsky, I. V.; Salazar-Alvarez, G.; Vasilakaki, M.; Trohidou, K. N.; Varela, M.; Stanley, D. C.; Sinko, M.; Pechan, M. J.; Keavney, D. J.; Peiró, F.; Suriñach, S.; Baró, M. D.; Nogués, J. *Nat. Commun.* **2013**, *4*, 2960.

(12) Song, Q.; Zhang, Z. J. *J. Am. Chem. Soc.* **2012**, *134*, 10182–10190.

(13) López-Ortega, A.; Estrader, M.; Salazar-Alvarez, G.; Roca, A. G.; Nogués, J. *Phys. Rep.* **2015**, *553*, 1–32.

(14) Lee, J. H.; Jang, J. T.; Choi, J. S.; Moon, S. H.; Noh, S. H.; Kim, J. W.; Kim, J. G.; Kim, I. S.; Park, K. I.; Cheon, J. *Nat. Nanotechnol.* **2011**, *6*, 418–422.

(15) Anil Kumar, P.; Ray, S.; Chakraverty, S.; Sarma, D. D. *Appl. Phys. Lett.* **2013**, *103* , 102406.

(16) Perumbilavil, S.; López-Ortega, A.; Tiwari, G. K.; Nogués, J.; Endo, T.; Philip, R. *Small* **2018**, *14*, 1701001.

(17) Hu, H.; Guan, B.; Xia, B.; Lou, X. W. *J. Am. Chem. Soc.* **2015**, *137*, 5590–5595.

(18) Sickafus, K. E.; Wills, J. M.; Grimes, N. W. *J. Am. Ceram. Soc.* **2004**, *82*, 3279–3292.

(19) O'Quinn, E. C.; Shamblin, J.; Perlov, B.; Ewing, R. C.; Neuefeind, J.; Feygenson, M.; Gussev, I.; Lang, M. *J. Am. Chem. Soc.* **2017**, *139*, 10395–10402.

(20) Tielens, F.; Calatayud, M.; Franco, R.; Recio, J. M.; Pérez-Ramírez; Minot, C. *J. Phys. Chem. B* **2006**, *110*, 988–995.

(21) Ndione, P. F.; Shi, Y.; Stevanovic, V.; Lany, S.; Zakutayev, A.; Parilla, P. A.; Perkins, J. D.; Berry, J. J.; Ginley, D. S.; Toney, M. F. *Adv. Funct. Mater.* **2014**, *24*, 610–618.

(22) Chiang, Y. M.; Wang, H.; Jang, Y. I. *Chem. Mater.* **2001**, *13*, 53–63.

(23) Muche, D. N. F.; Marple, M. A. T.; Hung, I.; Gan, Z.; Castro, R. H. R.; Sen, S. *J. Phys. Chem. C* **2017**, *121*, 13898–13905.

(24) Yang, A.; Chinnasamy, C. N.; Greneche, J. M.; Chen, Y.; Yoon, S. D.; Chen, Z.; Hsu, K.; Cai, Z.; Ziemer, K.; Vittoria, C.; Harris, V. G. *Nanotechnology* **2009**, *20*, 185704.

(25) Lüders, U.; Barthélémy, A.; Bibes, M.; Bouzehouane, K.; Fusil, S.; Jacquet, E.; Contour, J. P.; Bobo, J. F.; Fontcuberta, J.; Fert, A. *Adv. Mater.* **2006**, *18*, 1733–1736.

(26) Lin, C. C.; Tsai, Y. T.; Johnston, H. E.; Fang, M. H.; Yu, F.; Zhou, W.; Whitfield, P.; Li, Y.; Wang, J.; Liu, R. S.; Attfield, J. P. *J. Am. Chem. Soc.* **2017**, *139*, 11766–11770.

(27) Veal, T. D.; Feldberg, N.; Quackenbush, N. F.; Linhart, W. M.; Scanlon, D. O.; Piper, L. F. J.; Durbin, S. M. *Adv. Energy Mater.* **2015**, *5*, 1501462.

(28) Greenwald, S.; Pickart, S. J.; Grannis, F. H. *J. Chem. Phys.* **1954**, *22* , 1597.

(29) Gobbi, G. C.; Christoffersen, R.; Otten, M. T.; Miner, B.; Buseck, P. R.; Kennedy, G. J.; Fyfe, C. A. *Chem. Lett.* **1985**, *14*, 771–774.

(30) Armstrong, A. R.; Dupre, N.; Paterson, A. J.; Grey, C. P.; Bruce, P. G. *Chem. Mater.* **2004**, *16*, 3106–3118.

(31) Martins, F. H.; Silva, F. G.; Paula, F. L. O.; de A. Gomes, J.; Aquino, R.; Mestnik-Filho, J.; Bonville, P.; Porcher, F.; Perzynski, R.; Depeyrot, J. *J. Phys. Chem. C* **2017**, *121*, 8982–8991.

(32) López-Ortega, A.; Roca, A. G.; Torruella, P.; Petrecca, M.; Estradé, S.; Peiró, F.; Puntes, V.; Nogués, J. *Chem. Mater.* **2016**, *28*, 8025–8031.

(33) Tan, H.; Turner, S.; Yücelen, E.; Verbeeck, J.; Van Tendeloo, G. *Phys. Rev. Lett.* **2011**, *107*, 107602.

(34) de la Peña, F.; Berger, M.-H.; Hochepied, J.-F.; Dynys, F.; Stephan, O.; Walls, M. *Ultramicroscopy* **2011**, *111*, 169–176.

(35) Peña, F. de la; Ostasevicius, T.; Fauske, V. T.; Burdet, P.; Jokubauskas, P.; Nord, M.; Prestat, E.; Sarahan, M.; MacArthur, K. E.; Johnstone, D. N.; Taillon, J.; Caron, J.; Furnival, T.; Eljarrat, A.; Mazzucco, S.; Migunov, V.; Aarholt, T.; Walls, M.; Winkler, F.; Martineau, B.; Donval, G.; Hoglund, E. R.; Alxneit, I.; Hjorth, I.; Zagonel, L. F.; Garmannslund, A.; Gohlke, C.; Iyengar, I.; Chang, H.-W. **2017**.

(36) Stavitski, E.; de Groot, F. M. F. *Micron* **2010**, *41*, 687–694.

(37) Egerton, R. F. *Electron Energy-Loss Spectroscopy in the Electron Microscope (3rd Edition)*; Boston, MA, 2011.

(38) Yedra, L.; Xuriguera, E.; Estrader, M.; López-Ortega, A.; Baró, M. D.; Nogués, J.; Roldan, M.; Varela, M.; Estradé, S.; Peiró, F. *Microsc. Microanal.* **2014**, *20*, 698–705.

(39) Tan, H.; Verbeeck, J.; Abakumov, A.; Van Tendeloo, G. *Ultramicroscopy* **2012**, *116*, 24–33.

(40) Chardon, B.; Vigneron, F. *J. Magn. Magn. Mater.* **1986**, *58*, 128–134.

(41) El Mendili, Y.; Abdelouas, A.; Bardeau, J.-F. *Phys. Chem. Chem. Phys.* **2013**, *15*, 9197–9204.

(42) Jiang, M.; Peng, X. *Nano Lett.* **2017**, *17*, 3570–3575.

(43) Estradé, S.; Yedra, L.; López-Ortega, A.; Estrader, M.; Salazar-Alvarez, G.; Baró, M. D.; Nogués, J.; Peiró, F. *Micron* **2012**, *43*, 30–36.

(44) Varela, M.; Oxley, M. P.; Luo, W.; Tao, J.; Watanabe, M.; Lupini, a. R.; Pantelides, S. T.; Pennycook, S. J. *Phys. Rev. B - Condens. Matter Mater. Phys.* **2009**, *79*, 0851171-14.

(45) Torruella, P.; Arenal, R.; De La Peña, F.; Saghi, Z.; Yedra, L.; Eljarrat, A.; López-Conesa, L.; Estrader, M.; López-Ortega, A.; Salazar-Alvarez, G.; Nogués, J.; Ducati, C.; Midgley, P. A.; Peiró, F.; Estradé, S. *Nano Lett.* **2016**, *16*, 5068–5073.

(46) Laffont, L.; Gibot, P. *Mater. Charact.* **2010**, *61*, 1268–1273.

(47) Van Aken, P. a; Liebscher, B.; Styrsa, V. J. *Phys. Chem. Miner.* **1998**, *25*, 323–327.

(48) Colliex, C.; Manoubi, T.; Ortiz, C. *Phys. Rev. B* **1991**, *44*, 11402–11411.

(49) Schmid, H. K.; Mader, W. *Micron* **2006**, *37*, 426–432.

(50) Yedra, L.; Eljarrat, A.; Rebled, J. M.; López-Conesa, L.; Dix, N.; Sánchez, F.; Estradé, S.; Peiró, F. *Nanoscale* **2014**, *6*, 6646–6650.

(51) Torruella, P.; Arenal, R.; De La Peña, F.; Saghi, Z.; Yedra, L.; Eljarrat, A.; López-Conesa, L.; Estrader, M.; López-Ortega, A.; Salazar-Alvarez, G.; Nogués, J.; Ducati, C.; Midgley, P. A.; Peiró, F.; Estradé, S. *Nano Lett.* **2016**, *16*, 5068–5073.

(52) Shiga, M.; Tatsumi, K.; Muto, S.; Tsuda, K.; Yamamoto, Y.; Mori, T.; Tanji, T. *Ultramicroscopy* **2016**, *170*, 43–59.

(53) Yang, A.; Chen, Z.; Zuo, X.; Arena, D.; Kirkland, J.; Vittoria, C.; Harris, V. G. *Appl. Phys. Lett.* **2005**, *86*, 1–3.

(54) Lelis, M. F. F.; Porto, A. O.; Gonçalves, C. M.; Fabris, J. D. *J. Magn. Magn. Mater.* **2004**, *278*, 263–269.

(55) Carta, D.; Casula, M. F.; Falqui, A.; Loche, D.; Mountjoy, G.; Sangregorio, C.; Corrias, A. *J. Phys. Chem. C* **2009**, *113*, 8606–8615.

(56) Gholizadeh, A. *J. Am. Ceram. Soc.* **2017**, *100*, 3577–3588.

(57) Daou, T. J.; Pourroy, G.; Bégin-Colin, S.; Grenèche, J. M.; Ulhaq-Bouillet, C.; Legaré, P.; Bernhardt, P.; Leuvrey, C.; Rogez, G. *Chem. Mater.* **2006**, *18*, 4399–4404.

TOC.

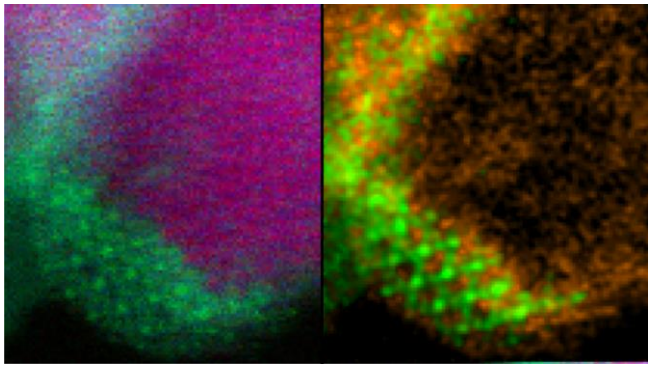

Supporting Information.

Atomic scale determination of cation inversion in spinel-based oxide nanoparticles.

Pau Torruella[1,2,*], Alicia Ruiz-Caridad[1,2,3], Michael Walls[3], Alejandro G. Roca[4], Alberto López-Ortega[5], Javier Blanco-Portals[1,2], Lluís López-Conesa[1,2,6] , Josep Nogués[4,7], Francesca Peiró[1,2], Sònia Estradé[1,2].

[1] LENS-MIND, Departament d'Enginyeria Electrònica i Biomèdica, Universitat de Barcelona, E-08028 Barcelona, Spain.

[2] Institute of Nanoscience and Nanotechnology (IN2UB), Universitat de Barcelona, E-08028 Barcelona, Spain.

[3] Laboratoire de Physique des Solides, Paris-Sud University, France

[4] Catalan Institute of Nanoscience and Nanotechnology (ICN2), CSIC and BIST, Campus UAB, Bellaterra, E-08193 Barcelona, Spain

[5] CIC nanoGUNE, Tolosa Hiribidea, 76, E-20018 Donostia-San Sebastián, Gipuzkoa, Spain

[6]TEM-MAT,CCiT, Universitat de Barcelona, E-08028 Barcelona, Spain.

[7] ICREA, Pg. Lluís Companys 23, E-08010 Barcelona, Spain.

* Corresponding autor: P. Torruella, e-mail: ptorruella@el.ub.edu

Preliminary EELS Characterization

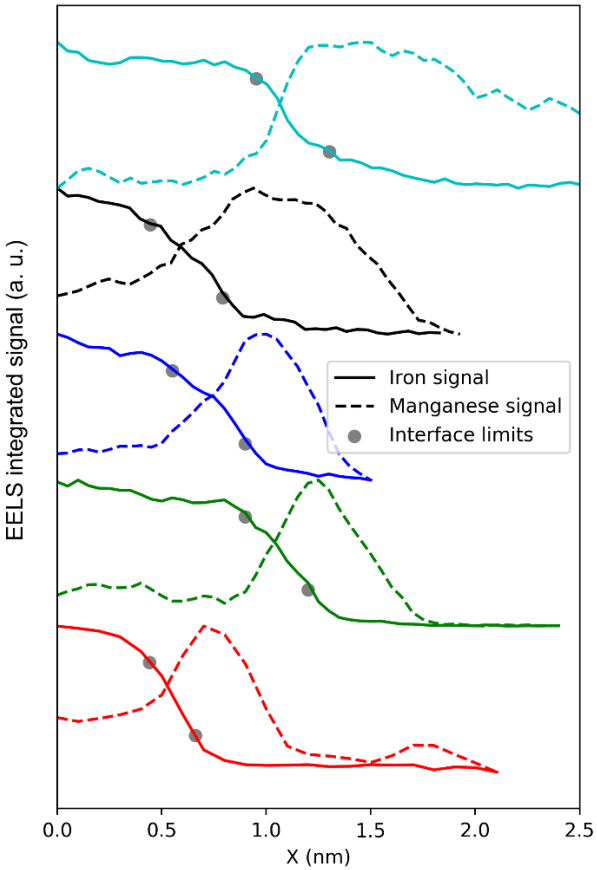

Figure S1. Fe $L_{2,3}$ and Mn $L_{2,3}$ edge integrated signals along core/shell interfaces of different nanoparticles. The interface limits were taken where Fe signal drops between 75% and 25% of the mean core signal.

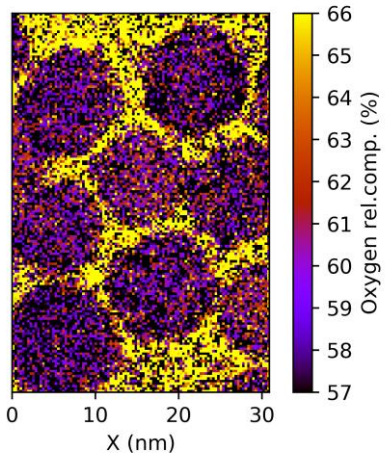

Figure S2. Oxygen relative composition from the spectrum image in Figure 1D-H, calculated through the Egerton quantification method[1].

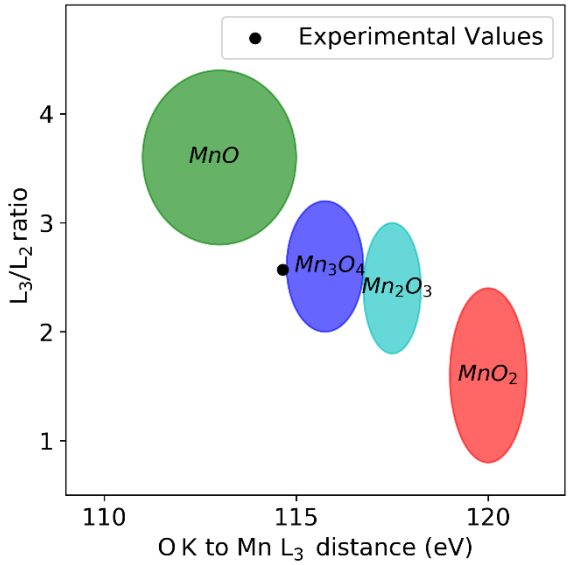

Figure S3. Comparison between the Mn $L_{2,3}$-edge ELNES parameters obtained from the nanoparticles (black dot) and the ranges of reported values for different Mn-oxides, calculated through the Oxide Wizard application[2].

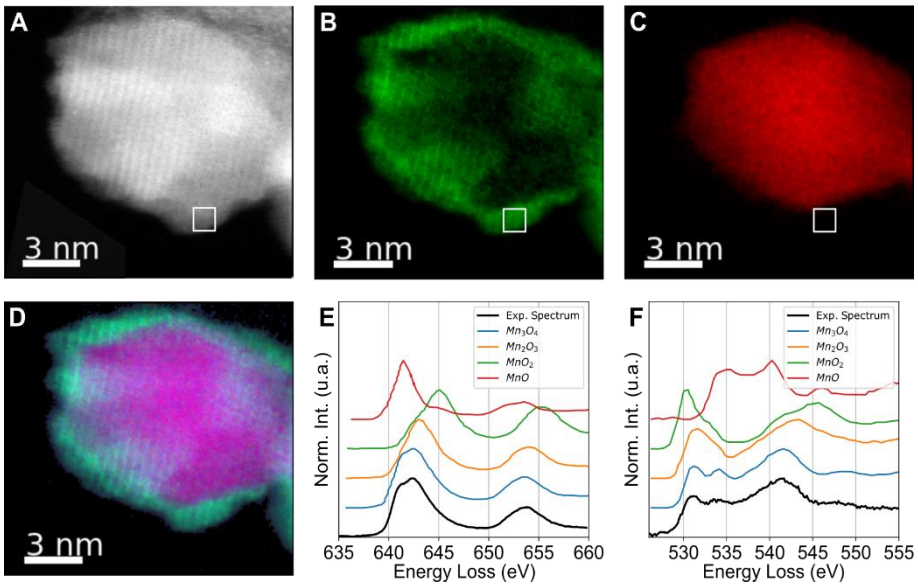

Figure S4. A) HAADF image. B) Mn signal. C) Fe signal. D) Color mix of the elemental signals. E) EELS spectrum in the region of the Mn L edge compared to data from[3]. F) O k edge compared to data from [3].

Crystal lattice assessment

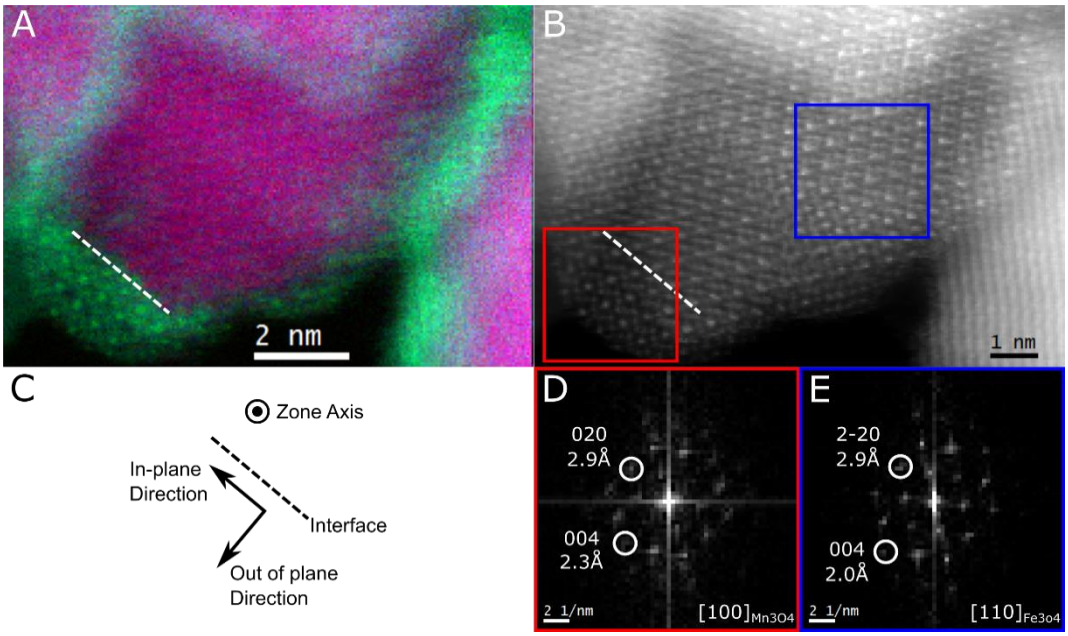

Figure S5. A) Mn (green) and Iron (red) and Oxygen(blue) signals. B)Atomic resolution STEM-HAADF image. The dotted line indicates the position of the interface. C) Scheme of the nomenclature used to describe the core/shell crystalline relations. D) FFT from the red region of panel A. The highlighted spots correspond to $(020)_{hausmanite}$, 2.9 Å, and $(004)_{hausmanite}$, 2.3 Å, seen along the $[100]_{hausmanite}$ zone axis. C) FFT from the blue region of panel A. The highlighted spots correspond to $(2\text{-}20)_{magnetite}$,2.9 Å, and $(004)_{magnetite}$, 2.0 Å, seen along the $[110]_{magnetite}$ zone axis.

The FFT from the center of the core/shell nanoparticle, highlighted in blue in Figure S5B, where the manganese signal is very low, matches excellently the Fe_3O_4 spinel crystal lattice[4], in agreement with the EELS characterization (Figure S5A). In particular, Figure S5E corresponds to a [110]Fe_3O_4 zone axis, where spots related to the (2-20)Fe_3O_4 (2.9 Å plane distance) and the (004)Fe_3O_4 (2.0 Å) planes can be observed (nominal spacing for these planes are $d(2\text{-}20)_{Fe3O4}$=2.968 Å and $d(004)_{Fe3O4}$=2.099 Å).

The FFT calculated from the shell region (in red in Figure S5B) corresponds to the [100] zone axis of the Mn_3O_4 Hausmanite phase[5] (Figure S5D). The 2.9 Å planes in figure S5D correspond to the (020)Mn_3O_4 and the 2.3 Å to the (004)Mn_3O_4 planes (nominal spacing for these planes are $d(004)_{Mn3O4}$ = 2.348 Å and $d(020)_{Mn3O4}$ = 2.870 Å, respectively).

In zone axis orientation, [001]Fe_3O_4//[001]Mn_3O_4 is are found perpendicular to the plane of the interface between the core and the shell referred to as out-of-plane direction (figure S5C). Accordingly, [1-10]Fe_3O_4//[010]Mn_3O_4 are found along the in-plane direction.

For the in-plane direction the lattice spacing in the shell region remains roughly the same as in the core, indicating an in-plane matching. For the out-of-plane direction, the lattice spacing is of 2.0 Å in the Fe_3O_4 core and 2.3 Å in the shell, indicating an expansion of up to 10% in the shell with respect to the core region.

The variations in lattice spacings of the crystal can be clearly visualized with Geometric Phase Analysis (GPA) (Figure S6). GPA is able to obtain maps of distortions in a crystal lattice with respect to a reference region. In this case, the reference region was chosen in the Fe_3O_4 core. Figure S6 shows GPA strain maps of the nanoparticle seen in the HAADF image of Figure S5B. The Exx image shows the strain along the in-plane direction (named X in the axis). The image Eyy reveals the strain along the out-of-plane direction (named Y in the axis). The map of strain in the X direction is essentially flat with only a planar defect showing up in the form a bright line in the map. This demonstrates that the manganese oxide lattice grows adapted to the magnetite core. To probe that the lattice expansion along Y was solely in the manganese shell region, a superposition of the strain map and HAADF image is provided in Figure S7.

The adaptation of the two lattices at the interface has an associated mismatch of $\frac{d(1-10)_{Fe_3O_4}-d(010)_{Mn_3O_4}}{d(1-10)_{Fe_3O_4}} = \frac{5.936\text{Å}-5.740\text{Å}}{5.936\text{Å}} = 3.3\%$. This, together with the fact that hausmanite has a tetragonal space group, should induce strong stresses and frustration in the shell when growing onto a (cubic space group) magnetite core. Consequently, it is no surprise to see planar defects in the nanoparticles (Figure S8). The STEM-Bright Field (BF) image in Figure S8A shows clear twinning planes at the surface in the three highlighted positions. A GPA strain map of the crystal (Figure S8B) highlights the three domains in which the crystal is divided. A second type of defect can be seen in Figure S8C where a stacking fault is present near the edge of the particle. The stacking fault becomes more visible in the corresponding GPA strain map (figure 8D). These two types of defects, both of which originate at the surface of the nanoparticles, are the most common among all the acquired images.

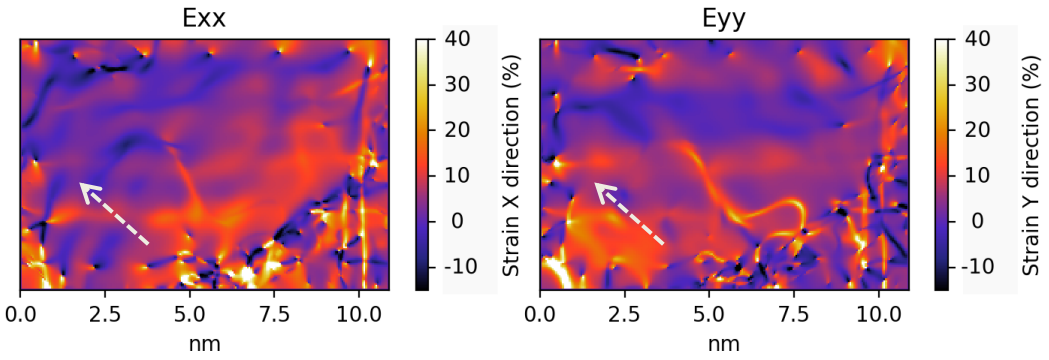

Figure S6. Geometric Phase Analysis (GPA) strain maps from Figure S5B. The Exx image maps the strain in the in-plane direction [1-10]Fe_3O_4//[010]Mn_3O_4 (X in the axis). The image Eyy maps the strain along the out-of-plane direction [001]Fe_3O_4//[001]Mn_3O_4 (Y in the axis). The dotted arrows indicate the position of the core/shell interface.

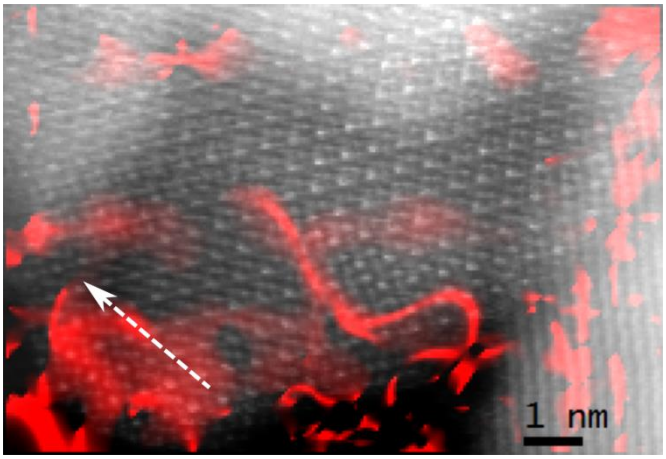

Figure S7. HAADF image (greyscale) superimposed on the Eyy GPA strain map (red) (strain perpendicular to the interface). The arrow indicates the core/shell interface.

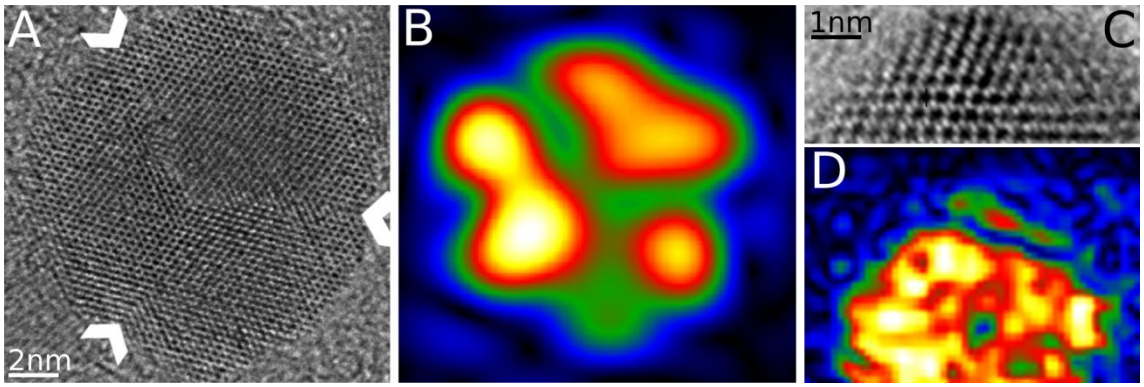

Figure S8. A) STEM-BF image of a nanoparticle. B) GPA phase map from panel A. C) STEM-BF image of the edge of a nanoparticle. D) GPA phase map from panel C.

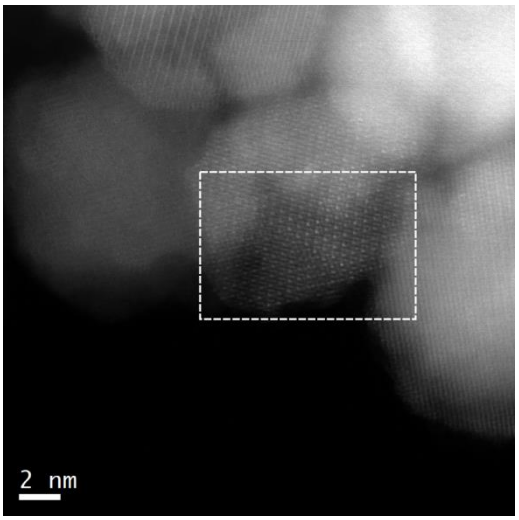

Figure S9. HAADF survey image for the EELS maps in Figure 2.

Cation inversion parameter calculation

When performing ELNES measurements in nanostructured materials, certain experimental issues can arise. For example, nanoparticles are usually in arbitrary zone axes, and signals from different ions and unit cells can be superimposed. Moreover, it is not always easy to obtain "absolute" data for some ELNES parameters. In particular, the position of an EELS edge may be offset by a detector-dependent value or by electron beam instabilities.

We propose to handle these problems by considering the shift in the EELS peak position instead of its absolute position cancelling any spectrometer misalignment. Also, if a linear relationship between the oxidation state and the L_3 peak position is assumed (reasonably for many transition metals[3]), the following expression for the spinel coordination inversion parameter can be derived:

$$x = \frac{2}{3}\left(1 - C\frac{S}{S_{ref}}\right)$$

Assuming (i) that an EELS spectrum is being acquired from a given atomic column, labeled by P, of a spinel oxide and (ii) that the energy value of a certain EELS edge (E_P) is given by theaverage between the value for 2+ ions (E^{2+}) and 3+ ions (E^{3+}) weighted by the number of atoms of each type in P. If in P there are A sites of tetrahedral oxygen coordination and B sites of octahedral oxygen coordination, and the coordination inversion parameter for that crystal is x, the expression for E_P is the following:

$$E_P = \frac{A(E^{2+}(1-x) + E^{3+}x) + B\left(E^{2+}\frac{x}{2} + E^{3+}(1-\frac{x}{2})\right)}{A+B}$$

Considering the position of the EELS edge for two columns (labeled 1 and 2), the EELS edge position shifts between column 1 and 2 by the following amount:

$$S \equiv E_{P_1} - E_{P_2} = \frac{A_1(E^{2+}(1-x) + E^{3+}x) + B_1\left(E^{2+}\frac{x}{2} + E^{3+}(1-\frac{x}{2})\right)}{A_1+B_1} - \frac{A_2(E^{2+}(1-x) + E^{3+}x) + B_2\left(E^{2+}\frac{x}{2} + E^{3+}(1-\frac{x}{2})\right)}{A_2+B_2}$$

From the previous expression, it is just a matter of rearranging terms to obtain the following expression for the cation inversion parameter:

$$x = \frac{2}{3}\left(1 - \frac{S}{S_{ref}}C\right)$$

Where $S_{ref} = E^{3+} - E^{2+}$and $C = \frac{(A_1+B_1)(A_2+B_2)}{B_1A_2 - A_1B_2}$.

Iron oxide core inversion

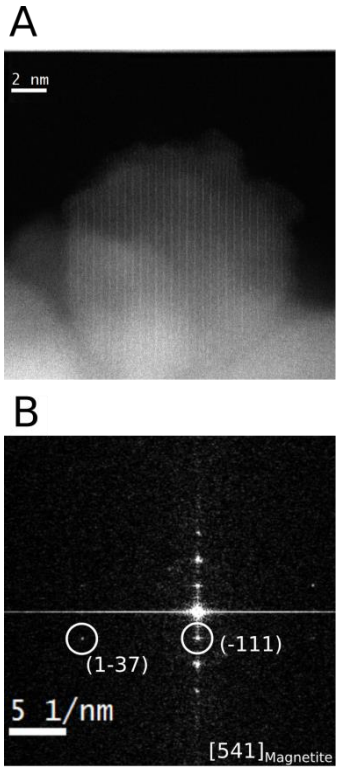

Figure S10. A) HAADF image and B) FFT with plane indexation of the nanoparticle in Figure 8.

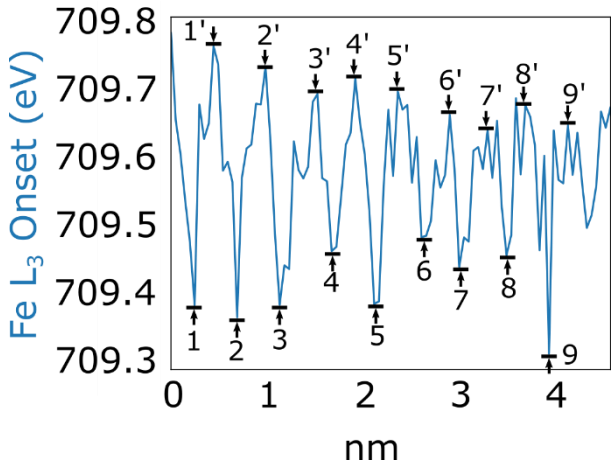

Figure S11. Measurements of Fe L3 shift from figure 3. The values obtained are 0.38 eV, 0.37 eV,0.31 eV,0.25 eV,0.32 eV,0.18 eV,0.22 eV,0.24 eV,0.35 eV resulting in an average value of 0.29 eV with a standard deviation of 0.07 eV.

MVA Spectral Decomposition

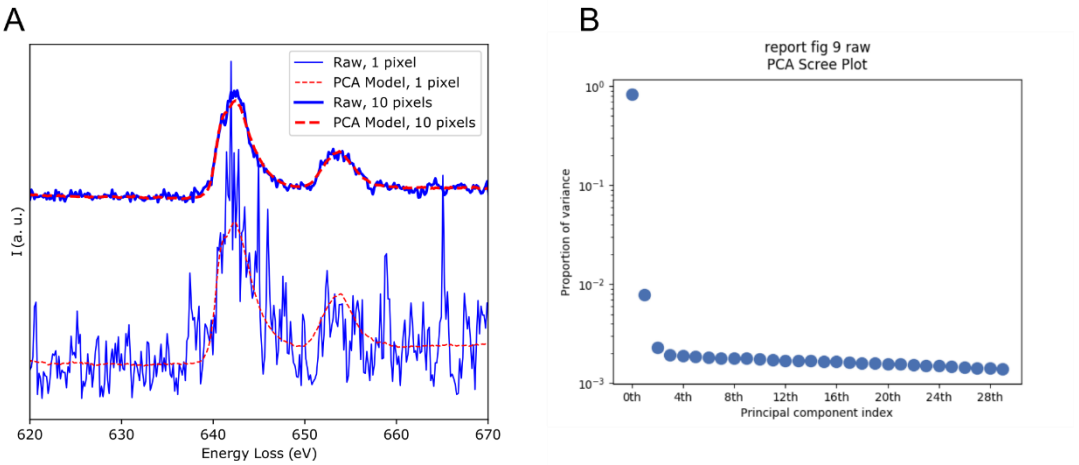

Figure S12.A) Comparison of raw data and PCA model for the spectra of 1 pixel and for the summed spectra of 10x10 pixels. B) Scree plot of the Mn edge PCA, where only 3 components stand out.

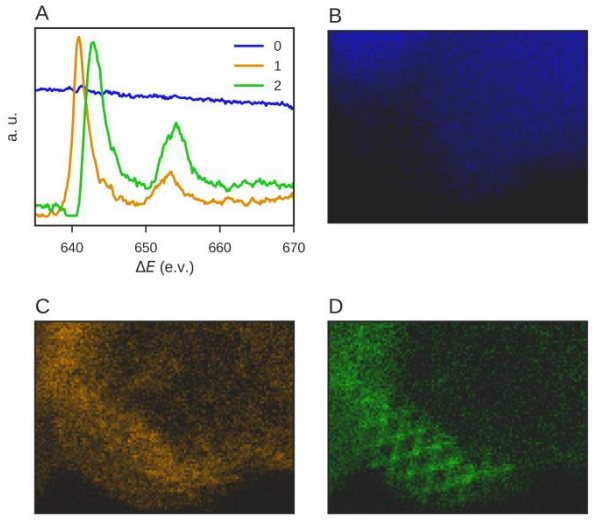

Figure S13. A) Spectral components obtained by NMF. B-D) the score maps associated with components 0-2.

X-ray absorption spectroscopy

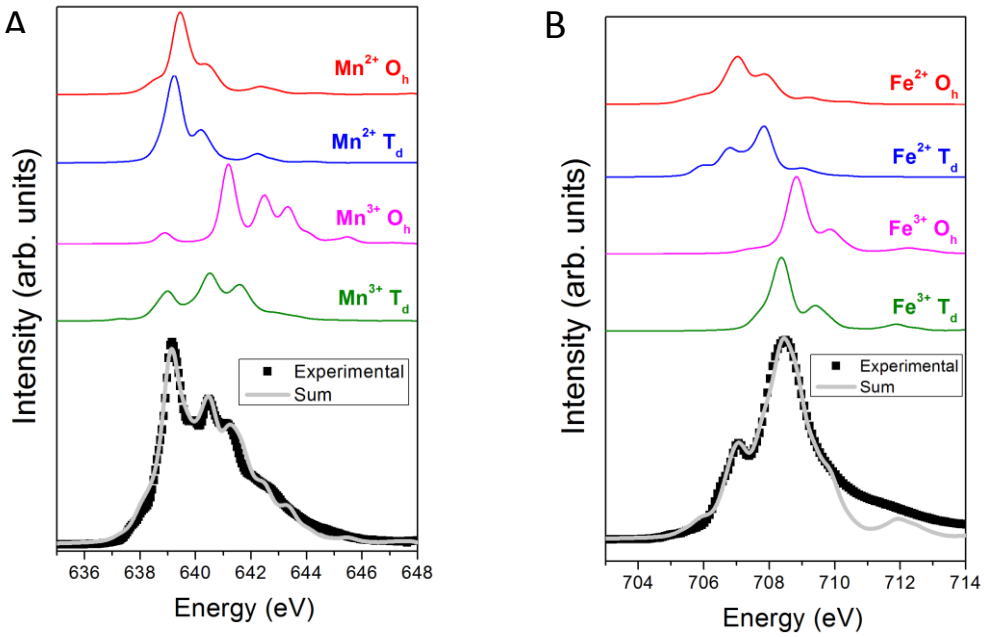

Figure S14. Experimental x-ray absorption spectra at the Mn (A) and the Fe (B) L_3-edge (symbols) and the corresponding simulation (gray line) obtained as a combination of the theoretical spectra of the 2+ and 3+ ions in either T_d or O_h environments (red, blue, magenta and green thin lines).

Table S1. Results of the Mn-edge simulation compared to the ones for nominal Mn_3O_4 (i.e., x = 0)

Mn L_3-edge	Number of ions for **x = 0**	% of ions for **x = 0**	Simulated number of ions	Simulated % of ions
Mn^{2+} O_h	0	0	0.44	15
Mn^{2+} T_d	1	33	0.56	19
Mn^{3+} O_h	2	66	1.56	51
Mn^{3+} T_d	0	0	0.44	15

Table S2. Results of the Fe-edge simulation compared to the ones for nominal Fe_3O_4 (i.e., x = 1)

Fe L_3-edge	Number of ions for **x = 0**	% of ions for **x = 0**	Simulated number of ions	Simulated % of ions
Fe^{2+} Oh	1	33	0.86	28
Fe^{2+} T_d	0	0	0.14	6
Fe^{3+} O_h	1	33	1.14	38
Fe^{3+} T_d	1	33	0.86	28

References

(1) Egerton, R. F. *Electron Energy-Loss Spectroscopy in the Electron Microscope (3rd Edition)*; Boston, MA, 2011.

(2) Yedra, L.; Xuriguera, E.; Estrader, M.; López-Ortega, A.; Baró, M. D.; Nogués, J.; Roldan, M.; Varela, M.; Estradé, S.; Peiró, F. *Microsc. Microanal.* **2014**, *20*, 698–705.

(3) Tan, H.; Verbeeck, J.; Abakumov, A.; Van Tendeloo, G. *Ultramicroscopy* **2012**, *116*, 24–33.

(4) El Mendili, Y.; Abdelouas, A.; Bardeau, J.-F. *Phys. Chem. Chem. Phys.* **2013**, *15*, 9197–9204.

(5) Chardon, B.; Vigneron, F. *J. Magn. Magn. Mater.* **1986**, *58*, 128–134.